# Development of Design Tools for Flow-Control Actuators

# Final Report

January 1, 2000 – December 31, 2003

Attention: Susan Gorton
Building 1247A, Room 210
Mail Stop 170
1A East Reid Street
Flow Physics and Control Branch
Fluid Mechanics and Acoustics Division
NASA Langley Research Center
Hampton, VA 23681-2199
Phone: (757) 864-5059
FAX : (757) 864-7897
email: S.A.GORTON@LaRC.NASA.GOV

*Prepared by:*

Jose Mathew, Quentin Gallas, and Louis N. Cattafesta III
Department of Aerospace Engineering,
Mechanics, and Engineering Science
University of Florida
P. O. Box 116250
Gainesville, FL 32611-6250
Email: catman@mae.ufl.edu
Phone: (352) 846-3017
Fax: (352) 392-7303

# Table of Contents

# 1 Overview

This report summarizes the activities on NASA Grant NAG-1-2249 during the past year. The work summarized below consists of two parts. The first part concentrates on the lumped element model of synthetic jets, while the second part focuses on the structural dynamic modeling of piezoceramic flap actuators.

## 1.1  Objectives

- Develop coupled electro/fluid/structural lumped-element model (LEM) of a prototypical flow-control actuator

- Validate the coupled electro/fluid/structural dynamics lumped-element models

- Develop simple, yet effective, design tools for actuators

- Develop structural dynamic models that accurately characterize the dynamic response of piezoelectric flap actuators using the Finite Element Method (FEM) as well as analytical methods

- Perform a parametric study of a piezo-composite flap actuator.

- Develop an optimization scheme for maximizing the actuator performance.

## 1.2  Progress

- Developed electro/fluid/structural models of piezoelectric-driven synthetic jet actuators using lumped-elements modeling

- Designed and fabricated a modular setup of a synthetic jet actuator driven by a piezoelectric-diaphragm to conduct careful experiments to isolate model components

- Designed optimized piezoelectric-diaphragms

- Developed structural dynamic model based on FEM for the design of piezoelectric flap actuators

- Designed, fabricated, and characterized the flap actuators

- Developed an analytical scaling method and an optimization scheme that enables to select the actuator parameters to maximize its performance for a given bandwidth.

## 2 Synthetic Jet Actuators

### 2.1 Theoretical Model of a Piezoelectric-Driven Synthetic Jet Actuator

A coupled electro-mechanical-acoustic model of a synthetic jet with piezoelectric-diaphragms was developed. The main assumption employed in lumped-element modeling (LEM) is that the characteristic length scale(s) of the governing physical phenomena are much larger than the largest geometric dimension. The governing equations for the distributed system are "lumped" into a set of coupled differential equations. Device components are represented by an equivalent circuit element and are connected by following specific rules based on the effort or flow variable type they share. The benefit of the LEM lies in the explicit relationship between each device component and the frequency response of the system. Such an approach provides a simple method to estimate the dynamic response of a synthetic jet and ultimately to design it.

The actuating diaphragm consists of a clamped axisymmetric piezoelectric unimorph actuator in which a piezoceramic is bonded to the central portion of a metal diaphragm. The composite diaphragm is driven into motion via an applied AC voltage. This represents a conversion from the electric to the mechanical domain. Since the primary purpose of the diaphragm is to produce large volume displacements, we focus on the first axisymmetric vibration mode of the composite diaphragm. To accomplish this, the diaphragm is lumped into an equivalent mass representing the stored kinetic energy and a compliance representing the stored potential energy. The

effective mechanical mass and compliance can be easily converted to their acoustic counterparts, and so it is convenient to treat the entire device as a couple electroacoustic system. Since the cavity contains a compressible gas, it too stores potential energy and it is modeled as an acoustic compliance. Finally, the orifice is a viscous region associated with motion of a fluid mass. Therefore, there will be an effective mass and a resistance associated with the orifice neck. The neck acoustic resistance takes into account the viscous loss in the neck and the non-linear discharge coefficient of the jet exit that is approximated by modeling the orifice as a generalized Bernoulli obstruction. For a first assumption, fully developed laminar pipe flow with oscillating pressure gradient is investigated to model the flow in the orifice. In addition, for low operational frequencies, a radiation mass is modeled, to first order, as a piston in an infinite baffle if the circular orifice is flush-mounted in a plate that is much larger in extent than the orifice radius.

The equivalent circuit representation of a synthetic jet is shown below. $M_{aM}$ and $C_{aM}$ are the acoustic mass and compliance of the piezo-diaphragm, respectively. $C_{aM}$ is the acoustic compliance of the cavity, while $R_{aO}$ and $M_{aO}$ are the acoustic resistance and mass of the orifice, respectively. $R_{aRad}$ and $M_{aRad}$ are the acoustic resistance and mass associated with the orifice radiation, respectively. The conversion from the electrical to the acoustic domains is accounted for via a transformer with a turns ratio $\phi_a$. This converts the driving current to a volume velocity of the diaphragm. The goal of the design is to maximize $Q_{out}/V_{AC}$ (i.e., the volume flow rate through the orifice per applied voltage).
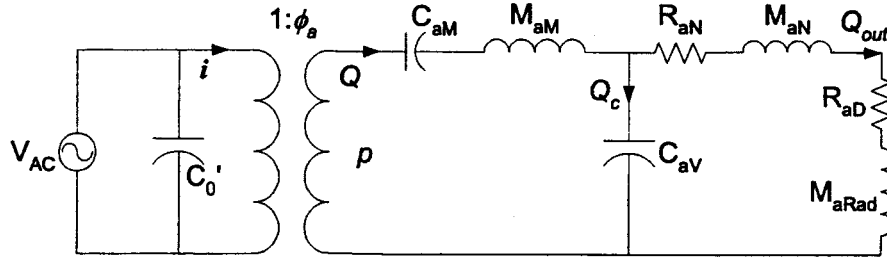
**Figure 1: Acoustical equivalent circuit representation of a piezoelectric-driven synthetic jet.**

The transfer function of the whole equivalent circuit is given by

$$\frac{Q_{out}}{V_{AC}} = \frac{s\phi_a C_{aM}}{a_4 s^4 + a_3 s^3 + a_2 s^2 + a_1 s + 1}, \text{ where}$$

$$
\begin{aligned}
a_1 &= (R_{aD} + R_{aN})(C_{aM} + C_{aV}) \\
a_2 &= (M_{aRad} + M_{aN})(C_{aM} + C_{aV}) + M_{aM}C_{aM} \\
a_3 &= C_{aV}M_{aM}C_{aM}(R_{aD} + R_{aN}) \\
a_4 &= C_{aV}M_{aM}C_{aM}(M_{aRad} + M_{aN})
\end{aligned}
\tag{1}
$$

Although this expression appears quite complex, it reveals some important features of the synthetic jet. First, the frequency response function is the ratio of volume velocity to the applied voltage. Since volume velocity is the derivative of the volume displacement, we see that for low frequencies ($s \to 0$), the volume velocity is zero and the volume displacement is $\phi_a C_{aM} = -d_a$, as expected. Second, the denominator is a 4$^{th}$-order polynomial in $s$, indicating two resonance frequencies. It can be shown that these two resonance frequencies are controlled by the diaphragm natural frequency $f_d$ and the Helmholtz frequency of the cavity $f_c$, given by

$$
\begin{aligned}
f_d &= \frac{1}{2\pi}\sqrt{\frac{1}{M_{aM}C_{aM}}} \\
f_c &= \frac{1}{2\pi}\sqrt{\frac{1}{(M_{aN} + M_{aRad})C_{aV}}}
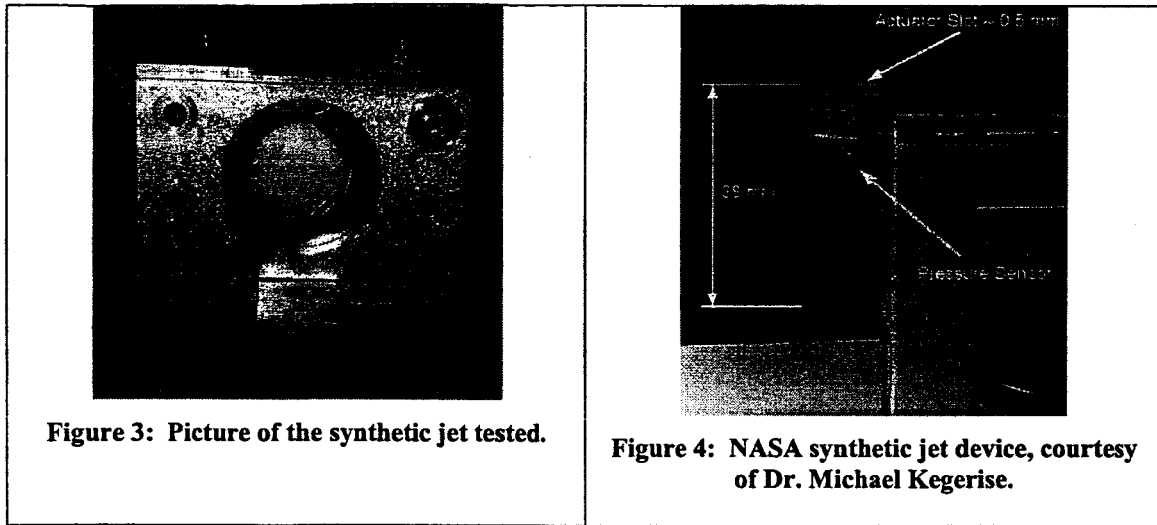\end{aligned}
\tag{2}
$$

such that

6

$$f_1 f_2 = f_d f_c \qquad (3)$$

## 2.2    Design of Modular Synthetic Jet Actuator

A modular apparatus of a piezoelectric-driven synthetic jet with cylindrical orifice was designed and constructed in order to perform careful experiments of each device component. The modular design allows for the interchanging of parts to test a variety of geometries, including the orifice, cavity, and different piezoelectric-diaphragms. Two mounts accommodate different composite piezoelectric-diaphragms (diameter of 27 mm or 41 mm, along with various thickness for both the piezoceramic and the shim). In addition a dual configuration can be obtained that is, two piezo-diaphragms are mounted face-to-face. The size of the cavity is modular in the same way with its height varying from 2 to 6 mm. Finally, various orifice plates provide an orifice with a diameter ranging from 0.28 mm to 0.78 mm and a depth from 0.5 to 2 mm. To mount the microphone flush against the bottom of the body plate, a tapered hole was machined from the end of the mount up to the cavity, which permitted insertion of the microphone without allowing air to escape. The basic device is shown below in Figure 2, along with one picture in Figure 3.
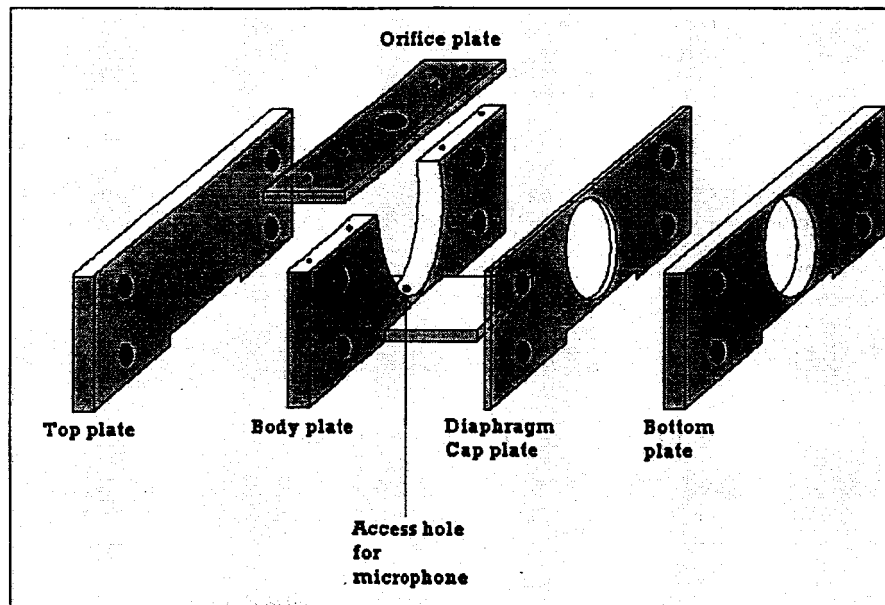
**Figure 2: Schematic of the modular synthetic jet apparatus.**



Figure 3: Picture of the synthetic jet tested.



Figure 4: NASA synthetic jet device, courtesy of Dr. Michael Kegerise.

In addition to this modular design, Dr. Michael Kegerise of NASA Langley provided us with the design drawing of a synthetic jet device that is currently under investigation, as shown above in Figure 4. This one differs essentially from the previous device by its rectangular slot, compared to the cylindrical orifice.

## 2.3    Experimental Procedures

In order to verify each component of the LEM, the experimental apparatus built permits a systematic parametric study of the synthetic jet design. The procedures are as follows:

- Piezoelectric-diaphragm excitation in a vacuum chamber to isolate the electromechanical coupling

- Oscillatory pressure in a sealed cavity to eliminate orifice effects

- Behavior of synthesized jets versus various orifice geometries to determine the orifice impedance in ambient flow conditions

## 2.4    Experimental Results

To gain confidence in the use of LEM as a potential tool to optimize the design of synthetic jets, we applied the above LEM approach to the NASA synthetic jet design since preliminary performance data was already available for that device. The predicted frequency response function between the applied voltage and the output volume flow rate is shown in Figure 5. The predicted resonant frequencies are 435 and 1557 Hz, while the estimated natural frequencies of the cavity and diaphragm are 443 and 1527 Hz.

Figure 6 shows the results of hot-wire measurements conducted by NASA to characterize the maximum velocity. Two curves are shown, one each for the maximum RMS and maximum amplitude of the velocity measured near the slot. The agreement between the LEM and the experiment is quite promising. It can be noted that, due to the lumped nature of the LEM, only the average velocity can be estimated. Clearly, the magnitude of the response at the resonance frequencies is not predicted correctly. This is undoubtedly due to the oversimplification of the resistance terms in $R_{aO}$. Nonetheless, the LEM predicts, using a driving AC voltage of 112 V, an *average* velocity in the range of 800-1000 Hz of approximately 8 m/s. This is in good agreement with experiment.
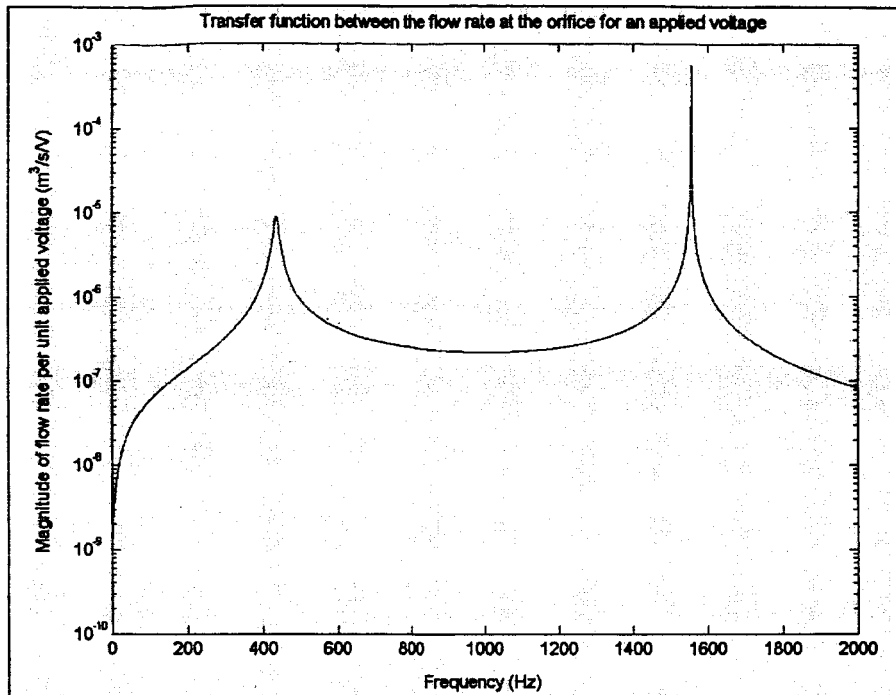
**Figure 5: LEM prediction of the frequency response of the synthetic jet actuator.**
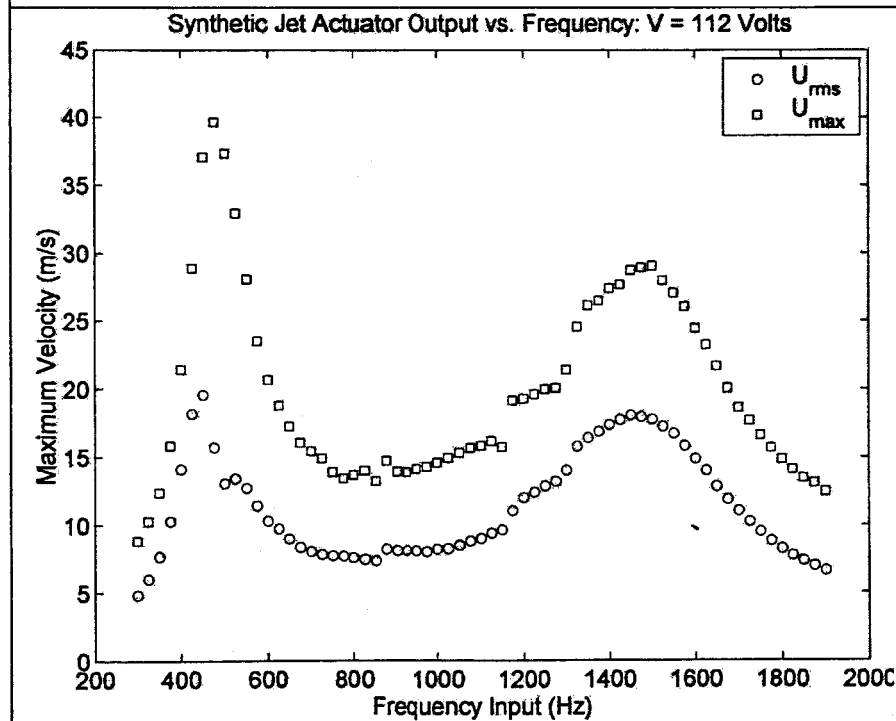


**Figure 6: Hot-wire measurment of the velocity response of the synthetic jet actuator. (Courtesy of Dr. Michael Keregise, NASA LaRC).**

Also, experiments of the piezoelectric-diaphragm itself were conducted to validate the composite linear plate theory used to model it. A maximum input voltage of 5 V drove the piezoelectric-diaphragm into motion, at a frequency on the order of 100~200 Hz, and the deflection of the diaphragm were measured by a scanning laser vibrometer. Figure 7 below shows the comparison between the experiment and the theory.

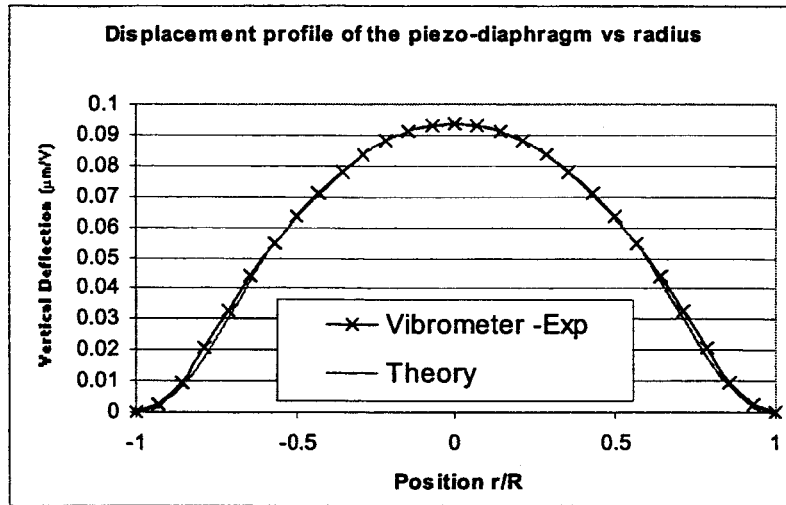**Displacement profile of the piezo-diaphragm vs radius**

Figure 7: Volume displacement of the piezoelectric-diaphragm by applied voltage.

Similarly, to test the theory on the cavity acoustic compliance, the orifice was replaced with a solid cap to provide a closed cavity and all leaks were carefully minimized. The piezoceramic was then driven with a nominal 1 V amplitude sinusoid, and the displacement of the vibrating diaphragm was measured with a laser displacement sensor (Micro-Epsilon Model ILD2000-10). A 1/8 in. Brüel & Kjær (B&K) type 4138 condenser microphone with B&K type 2669 preamplifier measured the fluctuating pressure in the closed cavity. The amplitude of the sinusoid was adjusted to avoid harmonics. The frequency response function between the pressure and displacement signal at the diaphragm center $w_0$ was used to measure $P/w_0$ at several frequencies and calculate $C_{aV}$, as shown in Figure 8. Using the average measured value of 9.89 $MPa/m$ and the measured mode shape, the cavity volume was determined to be

11

2.53x10-6 $m^3$ ± 12%. This nominal value is within ~1% of the cavity volume calculated from the geometry.
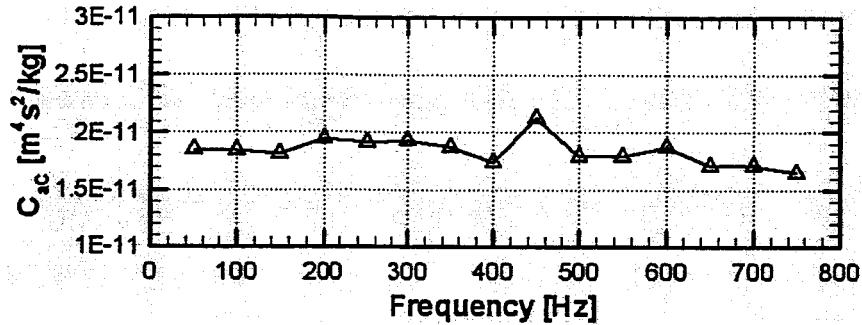


**Figure 8: Measured acoustic compliance $C_{aV}$ vs. frequency in closed cavity of synthetic jet.**

Finally, the lumped element model is used to predict the frequency response of two prototypical synthetic jet actuators. The dimensions and material properties of the piezoceramic diaphragms and actuator devices, along with the pertinent lumped element parameters, can be found in details in Gallas et al. (2003). Figure 9 show the model prediction of the centerline velocity compared to phase-locked LDV measurements versus frequency.
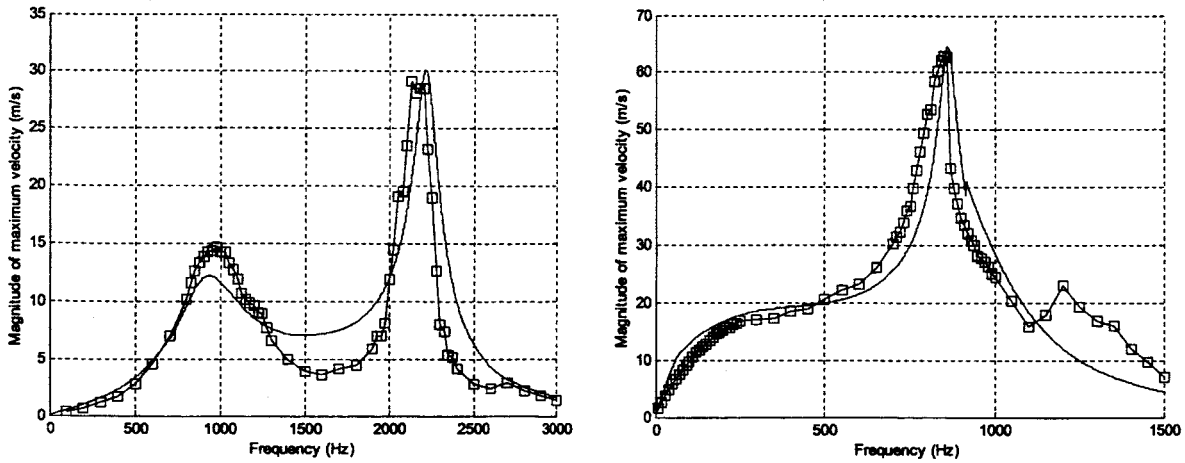


**Figure 9: Comparison between the lumped element model and experimental frequency response measured using phase-locked LDV for two prototypical synthetic jets (Gallas et al. 2003).**

## 2.5    Future Work

Future work will focus on the validation of each device component. Furthermore, we need to look in the acoustic liner literature for model improvement of the orifice behavior, including

nonlinear and grazing flow effects. In the same way, experiments and LEM results will be comparing with ongoing CFD simulations of the orifice flow conducted by Dr. Rajat Mittal of GWU. Once the LEM approach is validated, it will be used as basis for a synthetic jet design tool for end users utilization.

## 2.6    Publications/Presentations

Gallas, Q., Holman, R., Nishida, T., Carroll, B., Sheplak, M., and Cattafesta, L., "Lumped Element Modeling of Piezoelectric-Driven Synthetic Jet Actuators," *AIAA Journal,*.Vol. 41, No. 2, pp. 240-247, February 2003.

Gallas, Q., Mathew, J., Kaysap, A., Nishida, T., Sheplak, M., and Cattafesta, L., "Lumped Element Modeling of Piezoelectric-Driven Synthetic Jet Actuators, AIAA Paper 2002-0125, 40th AIAA Aerospace Sciences Meeting & Exhibit, January 2002.

Gallas, Q., Sheplak, M., and Cattafesta, L., "Lumped Element Modeling of Synthetic Jets, Ultra-Efficient Engine Technology Forum, NASA Glenn Research Center, September 2001.

# 3 Piezoelectric Flap Actuators

Piezoelectric flap actuators are desirable for active flow control applications. An understanding of their characteristics is essential prior to using them in a fluid flow. This portion of the report summarizes the theoretical modeling and experimental validation of the dynamic response of piezoelectric unimorph actuators. Two different finite element models (FEM) of a piezoelectric unimorph actuator are developed. One is a beam model that assumes a perfect bond exists between the piezoelectric patch and the shim, and the second extends the perfect bond model by incorporating a linear elastic shear element for the bond layer. These models are then used to predict the magnitude of the dc response (i.e., tip displacement per unit applied voltage) and the natural frequency of a piezoelectric flap. Also an approximate analytical static

model was developed to determine the functional dependence of the system response on the actuator parameters. The analytical model was also extended to study the response of bimorph actuators. The results are compared with experimental data obtained from a parametric study, in which ten otherwise identical piezoelectric flaps with varying piezoelectric patch sizes are fabricated and characterized using a laser displacement sensor. The results indicate that the theoretical models provide good estimates for the dc response and for the natural frequency when a linear elastic bond layer is used and a clamped boundary condition is realized. In particular all models produce estimates that are accurate to within 15% and 10% for the dc response and natural frequency, respectively. Finally a design procedure for developing actuators with optimum performance is briefly summarized.

### 3.1 Theoretical Model of a Piezoelectric-Driven Flap Actuator

A parametric study was carried out in which the geometry of a piezoelectric-shim was varied from approximately 10% to 100% of the total beam length in ten equal steps (while all other variables were fixed). The flaps were constructed of an aluminum alloy shim, with the piezoelectric material firmly affixed to its surface using an epoxy adhesive to form a piezo-composite beam. Figure 3 shows the schematic of a piezoelectric flap unimorph actuator. The total length of the shim is $L_T$ (~70 mm), the width is $b$ (~26 mm), and the thickness is $t_s$ (508 μm). A piezoceramic of length $L_p$ (variable) and thickness $t_p$ (254 μm) is bonded to the shim using an epoxy adhesive of thickness $t_b$ (13–25 μm). A small gap of length $L_{gap}$ (< 1 $mm$) is maintained between the clamp and the piezoelectric to eliminate stress concentrations and to prevent an electrical short circuit. Upon application of an external voltage to the piezoelectric electrode, the flap deflects in a direction determined by the orientation of the piezoelectric polarization vector with respect to the electric field.

14

In order to characterize piezoelectric flap actuators, a structural dynamics model is required that can accurately predict the frequency response of the flaps. Since flow-control applications of interest typically demand a large volume displacement, attention is restricted to the first bending mode only, which corresponds to the maximum volume displacement. Below, a "perfect bond" model and a "shear lag" model, both of which utilize finite element methodologies are used to calculate the frequency response of the actuators to an applied voltage. A simpler analytical static analysis is then described that is suitable for design.

The quantities of interest, namely the dc response and natural frequency of the actuator were calculated using the FEM and scaling analysis, and compared with the experimental results.
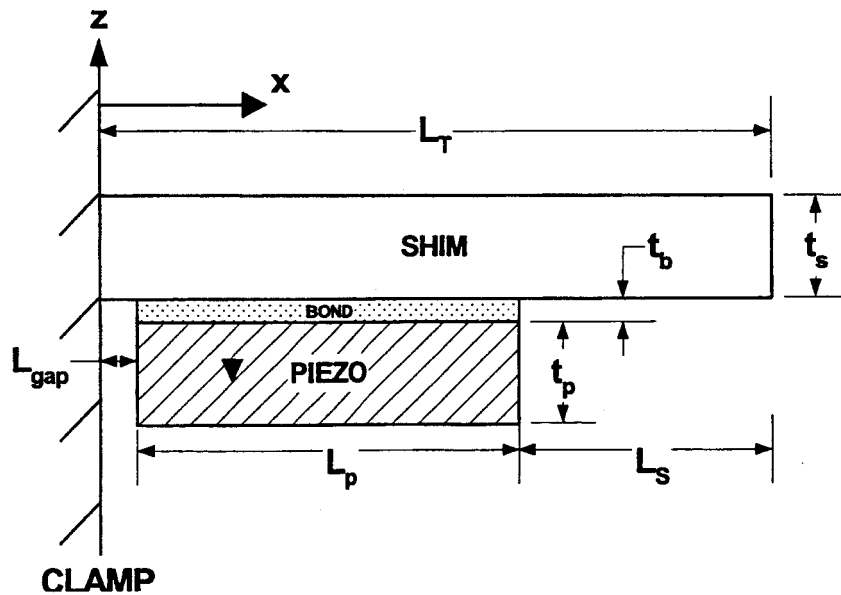
Figure 3: Flap actuator model.

## 3.2    Perfect Bond Finite Element Model

A simple schematic of the perfect bond model is shown in Figure 4. This assumes an infinitely rigid bond exists between the piezoelectric and the shim. All loads applied to the bond by the piezoelectric are transmitted fully to the shim.

Crawley and de Luis [1987] showed that a perfect bond between the piezoelectric and the shim leads to a concentrated couple or moment $M_o$ at the edges of the piezoelectric patch $x = L_{gap}$ and $L_p + L_{gap}$. As described in Cattafesta et al. [1997], a relationship can be obtained between the applied voltage and $M_o$, assuming that the actuator is in pure bending, and is given by

$$M_o = -\frac{1}{2} E_p d_{31} E_{field} b t_p \left( 2c_2 - t_p \right) \tag{4}$$

where $E_p$ is the elastic modulus of the piezoelectric, $d_{31}$ is the appropriate piezoelectric constant for a bender configuration, $E_{field}$ is the magnitude of the applied electric field, $b$ is the width of the flap, $t_p$ is the piezoelectric thickness, and $c_2$ is the location of the neutral axis in the composite section with respect to the bottom surface of the piezoelectric and is given by

$$c_2 = \frac{1}{2} \left[ t_p + t_s \frac{1 + \frac{t_p}{t_s}}{1 + \frac{E_p t_p}{E_s t_s}} \right], \tag{5}$$

where $E_s$ is the elastic modulus of the shim and $t_s$ is the shim thickness.
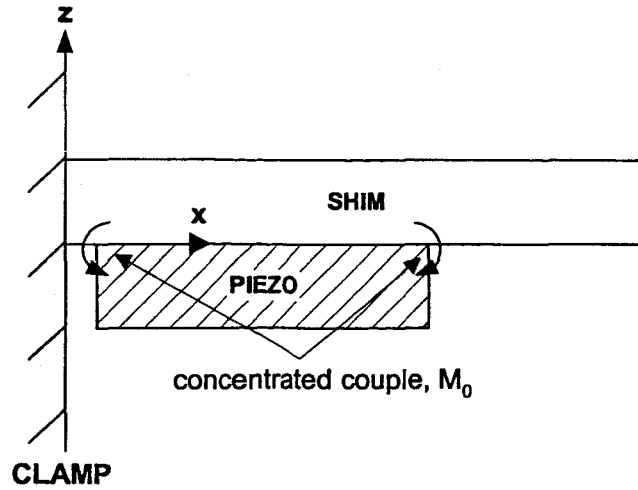
**Figure 4: Perfect bond model.**

It is important to note that a perfect bond cannot be achieved in practice because of the finite stiffness of the bond. Hence, a shear stress exists at the bond interface. This situation is considered in the next section.

A standard Euler-Bernoulli beam finite element model was developed to calculate the grid-resolved frequency response function for the piezoelectric actuators. The details of the finite element modeling scheme are given in Cattafesta et al. [2001]. The material properties of the flap are summarized in Table 1.

**Table 1: Flap Actuator Properties.**

| Property | AL-2024 (Aluminum shim) | PZT-5H (piezoceramic) | Eccobond 45 (Adhesive) |
|---|---|---|---|
| Elastic Modulus (Pa) | $7.33 \cdot 10^{10}$ | $6.2 \cdot 10^{10}$ | $3.98 \cdot 10^{8}$ |
| Density (kg/m$^3$) | 3290 | 7500 | 1060 |
| Piezoelectric constant (m/V) | N/A | $-274 \cdot 10^{-12}$ | N/A |
| Shear Modulus (Pa) | N/A | N/A | $1.48 \cdot 10^{8}$ |

## 3.3    Shear Lag Finite Element Model

The perfect bond model described above results in an artificially stiff model for the flap actuator, causing predicted values for the natural frequency that are higher than the corresponding measured values (Cattafesta et al. [2001]). A more realistic model for the bond is thus sought to obtain better quantitative predictions for the flap characteristics.

A perfect bond model neglects the presence of the bonding adhesive layer between the aluminum shim and the piezoelectric. The bond layer is viscoelastic to some extent and possesses a finite stiffness. Some amount of strain will occur in the bond layer, resulting in a shear lag between the induced strain by the piezoelectric and the strain actually transmitted to the shim via the bond layer.

Crawley and de Luis [1987] showed that the maximum shear stress occurs near the two edges of the piezoceramic patch, whereas the shear stress distribution is almost zero for the remaining regions of the bond. The stress distribution also has opposite signs at the two edges of the bond. The shear-lag model described below represents an extension of their work to investigate the effect of the bond layer on the dynamic response of the actuators.

A schematic of the shear lag model is shown in Figure 5. Due to the deformation of the piezoelectric induced by the application of an external electric field, a horizontal electromechanical force of magnitude $f = d_{31} E_{field} E_p A$ acts on the front and back faces of the piezoelectric section, where $E_p$ is the elastic modulus and $A = bL_p$ is the cross-sectional area of the piezoelectric. A shear stress $\tau(x)$ acts at the interface between the bond and the piezoelectric (and the bond and shim), as shown in Figure 5. A free-body diagram of the piezoelectric reveals the relationship between the magnitudes of $f$ and $\tau(x)$, $f = \int_0^{L_p/2} \tau(x) b \, dx$. An inspection of Figure 4 for the perfect bond case reveals the effect of this force is to produce an induced couple in Eq. (4). The relation between the horizontal electromechanical force and the induced couple can be obtained by combining Eq. (4) with the definition for $f$ and is given by the formula

$$f = \frac{-L_p M_0}{\left(2c_2 - t_p\right)t_p} \tag{6}$$

Thus, the flap deflects or bends upon application of a voltage, and the direction of motion is determined by the orientation of the piezoelectric polarization vector with respect to the electric field. The net effect is that a finite shear stress or shear lag, $\tau(x) = G\left(\partial u / \partial z\right)$, is induced in the bond layer due to the deformation of piezoelectric, resulting in a decreased induced strain being

transmitted to the shim. Here, $u$ is the displacement in the $x$ direction and $G$ is the rigidity modulus.

A finite element model, similar to the one used for the perfect bond model, was developed. The solution procedure is same as that for the perfect bond model, the details of which are given in Mathew et al. [2001].
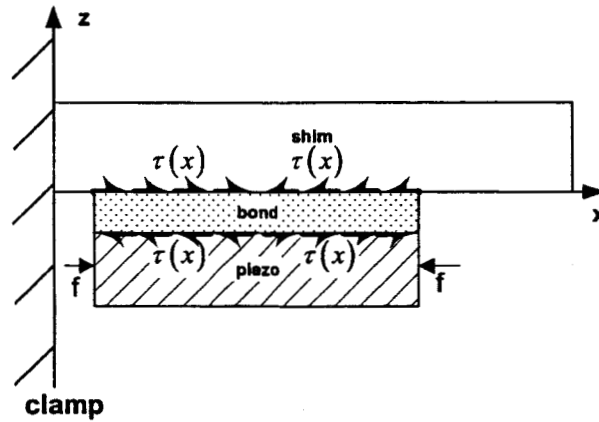
**Figure 5: Shear lag model.**

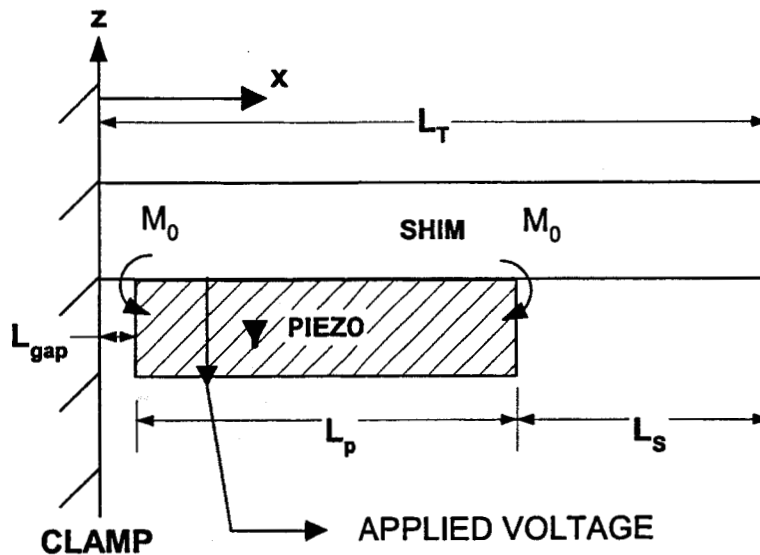## 3.4 Analytical Scaling Analysis

**Figure 6: Schematic of unimorph piezoelectric flap composite beam.**

In order to obtain the functional dependence of the critical quantities like dc response and natural frequency on the flap design parameters, an analytical scaling analysis was undertaken. The sections below briefly summarize the modeling scheme used.

### 3.4.1 Calculation of dc response

The Euler-Bernoulli beam equation for the flap was solved for an applied external voltage. Figure 6 shows the arrangement of a unimorph piezoelectric patch that is perfectly bonded to a shim material. The application of a voltage produces a couple that acts at the edges of the piezoelectric patch, as described in the perfect bond model. The composite beam is split into three sections. Section 1, of length $L_{gap}$, is the small gap region between the clamp and the piezoelectric. Section 2, of length $L_p$, is the composite section. Section 3, of length $L_s$, is the second shim section.

In Section 1, the governing static equilibrium equation for the vertical deflection of the beam is

$$E_s I_{s_1} \frac{d^2 w_1}{dx^2} = M_1 = 0. \tag{7}$$

In Section 2, the governing static equilibrium equation is given by

$$E_s I_{s_2} \frac{d^2 w_2}{dx^2} + E_p I_{P_2} \frac{d^2 w_2}{dx^2} = M_0, \tag{8}$$

where $M_0$ is due to the applied voltage and is given by Eq. (4). In Section 3, the governing static equilibrium equation is given by

$$E_s I_{s_3} \frac{d^2 w_3}{dx^2} = M_3 = 0. \tag{9}$$

To find the beam deflection as a result of an applied electric field, we use the following four boundary conditions for a cantilever beam

21

$$w_1(x=0)=0,$$
$$w_1'(x=0)=0,$$
$$w_3''(x=L_T)=0,$$

and

$$w_3'''(x=L_T)=0. \tag{10}$$

These boundary conditions states that the deflection and slope are zero at the clamped edge and the force and moment are zero at the free edge. The matching condition matches the deflection and slope at the interface between sections

$$w_1(x=L_{gap})=w_2(x=L_{gap}),$$
$$w_1'(x=L_{gap})=w_2'(x=L_{gap}),$$
$$w_2(x=L_{gap}+L_p)=w_3(x=L_{gap}+L_p),$$

and

$$w_2'(x=L_{gap}+L_p)=w_3'(x=L_{gap}+L_p). \tag{11}$$

In the ideal case the gap region is negligible in size and neglected, $L_{gap} \to 0$, so we can write the piecewise continuous beam deflection equation as

$$w_1(x)=0, \qquad\qquad 0 \le x \le L_{gap}$$
$$w_2(x) \cong \frac{M_2}{(EI)_c}\frac{x^2}{2}, \qquad L_{gap} \le x \le L_{gap}+L_p$$

and

$$w_3(x) \cong \frac{M_2 L_p}{(EI)_c}\left(x-\frac{L_p}{2}\right). \qquad L_{gap}+L_p \le x \le L_T \tag{12}$$

To obtain the tip deflection, we substitute for $x=L_T$, $(EI)_c = E_s I_{s_2} + E_p I_{p_2}$, and the expression for $M_2$ from Eq. (4) into the expression for $w_3(x)$

22

$$w_{tip} \cong -\frac{-3E_p t_s \left(t_s + t_p\right) E_s L_p \left(L_p - 2L_T\right) d_{31} V}{\left(E_s^2 t_s^4 + 4E_s t_s^3 E_p t_p + 6E_p t_p^2 E_s t_s^2 + 4E_p t_p^3 E_s t_s + E_p^2 t_p^4\right)}. \tag{13}$$

It can be shown that the dc response depends on non-dimensional parameters like $t_p / t_s$, $L_p / L_T$,

$E_p / E_s$, $t_s / L_T$, and $d_{31} V / t_p$, where $E_{field} = V/t_p$. Define $\bar{t} = t_p / t_s$, $\bar{L} = L_p / L_T$ and $\bar{E} = E_p / E_s$

for the purposes of scaling the dc response. Substituting these into Eq. (13) and dividing by

$d_{31} V L_T / t_p$ gives

$$W = \frac{w_{tip} t_p}{d_{31} V L_T} \cong \frac{-3\bar{E}\left(1+\bar{t}\right)\bar{t}\left(\bar{L}-2\right)\bar{L}\dfrac{L_T}{t_s}}{\left(1+4\bar{E}\bar{t}+6\bar{E}\bar{t}^2+4\bar{t}^3\bar{E}+\bar{E}^2\bar{t}^4\right)}. \tag{14}$$

The above expression gives the tip deflection for a given piezoelectric material of a specified

total length for an applied electric field. The implications of the above expression will be

discussed at a later stage in this report.

A similar analysis as above can be done for a symmetric bimorph actuator. A bimorph

actuator has oppositely poled piezoelectric patches attached to both sides of the shim and is used

in applications that require greater volume displacements. The schematic of a bimorph actuator

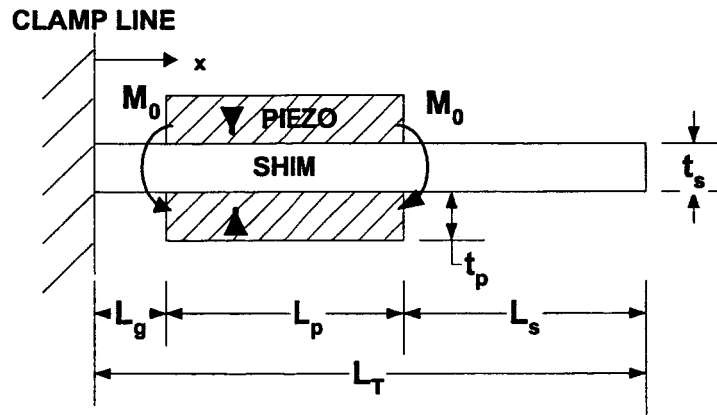is shown in Figure 7. The dimensioning convention is same as that for the unimorph actuator.



Figure 7: Schematic of a bimorph actuator.

The induced moment at the piezoelectric shim interface is given by the general expression

$$M_0 = \int y\sigma(y)dA \qquad (15)$$

where $y$ is the coordinate along the cross section measured from the neutral axis, $\sigma(y)$ is the normal stress distribution, and $dA$ is the area element for integration. Eq. (15) can be simplified to

$$M_0 = -E_p t_p d_{31} E_{field} bt_s \left( \frac{t_p}{t_s} + 1 \right) \qquad (16)$$

Note that the neutral axis passes along the centroid of the cross-section. Following the same procedure as that for the unimorph, the non-dimensional tip deflection can be expressed as

$$W = \frac{w_{tip} t_p}{d_{31} V L_T} \cong \frac{-6\bar{E}(1+\bar{t})\bar{t}(\bar{L}-2)\bar{L}\dfrac{L_T}{t_s}}{\left(1 + 6\bar{E}\bar{t} + 12\bar{E}\bar{t}^2 + 8\bar{t}^3\bar{E}\right)}. \qquad (17)$$

### 3.4.2   Calculation of natural frequency

The natural frequency of the composite beam is calculated based on the static deflection of the composite beam under self load (i.e., weight). For simplicity, the gap region is neglected in this analysis. The schematic of the beam is given in Figure 8. In the figure, $q_2$ and $q_3$ are the load per unit length of the composite section and the shim section respectively.
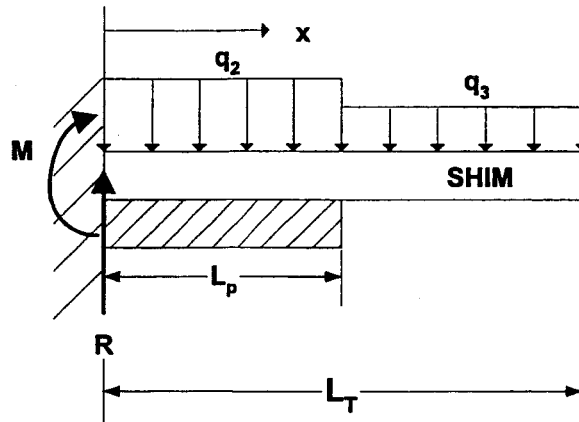


Figure 8:  Schematic of the beam under self load.

A free body analysis of the beam gives the force and moment acting at the clamp point as

24

$$R = q_2 L_p + q_3 \left( L_T - L_p \right) \tag{18}$$

$$M = -\left( \frac{q_2 L_p^2}{2} + \frac{q_3 \left( L_p^2 + L_T^2 \right)}{2} \right) \tag{19}$$

Using the same nomenclature described in the previous analysis, the governing equation for vertical deflection in Section 2 is given as

$$\left( E_s I_{s_2} + E_p I_{P_2} \right) \frac{d^2 w_2}{dx^2} = M + Rx - q_2 \frac{x^2}{2}. \tag{20}$$

In Section 3, the governing static equilibrium equation is given by

$$E_s I_{s_3} \frac{d^2 w_3}{dx^2} = -q_3 \frac{\left( x - L_T \right)^2}{2}. \tag{21}$$

To find the beam deflection as a result of an applied electric field, we use the same boundary conditions, Eq. (10), and matching conditions, Eq. (11). This result in the following piecewise continuous beam deflection relation:

$$w_2 (x) = \frac{-x^2}{24(EI)_c} \left( 6L_p^2 (q_1 - q_2) + 6q_2 L_T^2 - 4xq_1 L_p + 4xq_2 \left( L_p - L_T \right) + q_1 x^2 \right) \tag{22}$$

and

$$w_3 (x) = \frac{-1}{24(EI)_s} \left( Ax^4 + Bx^3 + Cx^2 + Dx + E \right), \tag{23}$$

where

$$A = q_2, B = -4q_2 L_T, C = 6q_2 L_T^2$$

$$D = \frac{(EI)_s}{(EI)_c} \left( 4q_1 L_p^3 + 12L_p q_2 L_T^2 - 12L_p^2 q_2 L_T^2 \right) + 12L_p q_2 L_T \left( L_p - L_T \right) - 4q_2 L_p^3 \tag{24}$$

$$E = L_p^2 \frac{(EI)_s}{(EI)_c} \left( 8q_2 L_p L_T - 2q_2 \left( L_p^2 + 3L_T^2 \right) - q_1 L_p^2 \right) + q_2 L_p^2 \left( 6L_T^2 - 8L_p L_T + 3L_p^2 \right)$$

The tip deflection for an applied force is given by the expression

$$w_{tip} = \frac{1}{24(EI)_c}\left(6q_2 L_p L_T^2\left(-2L_T+3L_p\right)+\left(L_p^4-4L_T L_p^3\right)\left(q_1+2q_2\right)\right)+$$

$$\frac{-3q_2}{24(EI)_s}\left(L_p^4+L_T^4-2L_p L_T\left(2L_T^2-3L_T L_p+2L_p^2\right)\right)$$

(25)

As a check, note that Eq. (25) reduces to $-3q_2 L_T^4/\left(24(EI)_s\right)$, which is the tip deflection of a cantilever beam under self load, for the limiting cases when $(EI)_s = (EI)_c$ and $L_p = 0$. The potential energy associated with the deflection in the beam is given by the expression

$$U = \frac{1}{2}\int_0^{L_T} E(x)I(x)\left(\frac{d^2w(x)}{dx^2}\right)^2 dx.$$

(26)

Similarly, the kinetic energy is given by the expression

$$T = \frac{1}{2}\int_0^{L_T} m_l(x)\left(\dot{w}(x)\right)^2 dx.$$

(27)

where $m_l(x)$ is the mass per unit length of the actuator. Integrating Eq. (26) and Eq. (27) using the piecewise continuous solution, Eq. (22)– Eq. (23), we obtain the total potential and kinetic energy of the beam. Lumping the potential energy and the kinetic energy at the tip, we can obtain the effective compliance and mass of the composite beam.

The effective compliance of the composite beam is

$$C_{eff} = \frac{\left(w_{tip}\right)^2}{2U}.$$

(28)

Similarly, the effective mass for the beam is obtained by the expression

$$M_{eff} = \frac{2T}{\left(\dot{w}_{tip}\right)^2}.$$

(29)

The first resonant frequency of the composite beam is estimated by

26

$$f_n = \frac{1}{2\pi} \sqrt{\frac{1}{C_{\textit{eff}} M_{\textit{eff}}}}. \qquad (30)$$

The natural frequency is estimated for both the unimorph and bimorph actuators. The expression for the natural frequency is very long and is therefore not listed here. The natural frequency can be normalized by the natural frequency of a homogenous beam under self load and is given by the formula

$$F = \frac{f_n}{0.1622} \sqrt{\frac{\rho_s L_T^4}{E_s t_s^2}}. \qquad (31)$$

It can be shown that the non-dimensional natural frequency is a function of non-dimensional parameters like $t_p / t_s$, $L_p / L_T$, $E_p / E_s$, and $\rho_p / \rho_s$.

## 3.5  Experimental Setup and Procedure

Experiments were conducted to characterize the piezoelectric actuators and obtain their natural frequency and dc response. The response of the actuators to an applied input voltage was measured. A laser displacement sensor was used to obtain the frequency response function between input voltage and output tip displacement.

The set of actuators designed had a typical length of 70 mm and a width of 26 mm. The shim was 508 μm thick, while the piezoelectric was 254 μm thick. The piezoelectric patch was firmly bonded to the shim using Eccobond 45 epoxy adhesive. Eccobond 45 epoxy has a glass transition temperature of $48^\circ$ and is not very viscoeleastic leading to minimal dissipation of energy as heat. The thickness of the bond layer varied slightly from 13–25 μm over the bonding area. Ten of these actuators were built, where the length of the piezoelectric patch was increased in steps of 10% between the successive actuators. The actuators were clamped at one end on a test apparatus to approximate a clamped-free boundary condition. Care was taken to ensure the rigidity of the clamp so that there is minimal motion at the base of the clamp when the actuator is

vibrating. The actuators were mounted vertically on the test apparatus and the electric lead connections were realized via low resistance (<10 ohms) strain-relieved, conductive copper tape attached to the piezoelectric patch as well as to the grounded apparatus.

A periodic sweep excitation signal was generated using a function generator (HP model E1441 A). The sweep signal spanned a frequency range from 0.1 to 200 Hz with amplitude of 0.05 V. The voltage signal was amplified by a nominal gain of 30 using a piezoelectric amplifier (PCB Model 790A06). The period of the chirp was set at 4 seconds to provide good frequency resolution ($\Delta f = 0.25$ Hz) for the spectral analysis. The output data was acquired using a 16-bit data acquisition system (HP model E1433A). Fifty block averages of the spectral data were found suitable to reduce the random error component to negligible levels. The laser beam was focused at a point approximately 1 mm from the midpoint of the tip of the flap. The schematic of the experimental setup is shown in Figure 9.
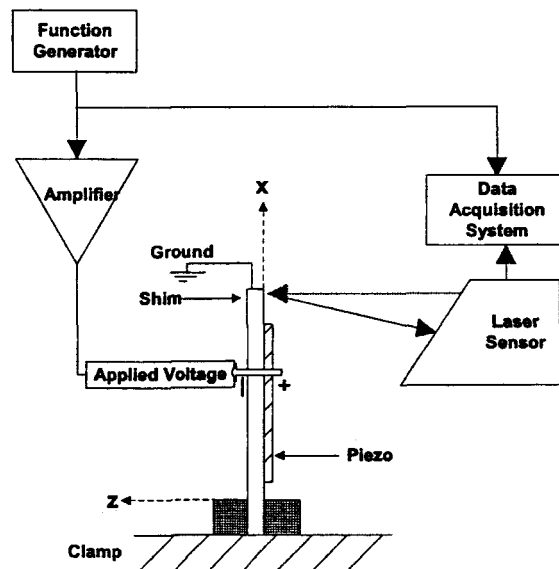


Figure 9: Schematic of the experimental setup.

28

## 3.6    Results and Discussion

A laser displacement sensor was used to characterize the actuators. The frequency response function of the actuators was measured and the natural frequency and dc response was calculated from the frequency response. The results were compared with the values obtained from the two finite element models as well as the analytical model described previously. The dc response was calculated from a $2^{nd}$-order system fit as well as from an average of first ten frequency response function magnitude values. The mathematical expression for the fit is given as

$$H(\omega) = \frac{X(\omega)}{V} = \frac{1}{-M\omega^2 + Cj\omega + K} \tag{32}$$

where the frequency response function fit, $H(\omega)$, is defined as the ratio of the tip displacement $X(\omega)$ to the applied voltage $V$, for each frequency $\omega$. The coefficients $M$, $C$, and $K$ are the effective mass, damping and stiffness for the system respectively. The natural frequency was calculated from a $90^{\circ}$ phase angle, the frequency corresponding to the peak of the power spectral density, theoretical fit, and an impact hammer test. The response of the actuators was calculated using multiple methods to obtain a good agreement between experiment and theoretical values. The details of these multiple methods for the calculation of dc response and natural frequency are given in Mathew [2002].

A comparison of the natural frequency for the flaps between experiment and theoretical values is plotted versus normalized piezoelectric length in Figure 10. The experimental results agree well with the theory to within +/- 10%. Theoretical values include predictions from the analytical model, perfect bond finite element model analysis and shear-lag finite element model analysis. The prediction from the shear lag model is closest to the experimental values. The perfect bond frequency predictions are higher than the shear lag values, while the static analysis data serves as an upper limit for the theoretical predictions. Note that analytical model gives

identical results to the perfect bond finite element model if $L_g \neq 0$ is not assumed. A peak in the system bandwidth is observed for $L_p/L_T \cong 0.5$. For low values of $L_p/L_T$, increasing $L_p/L_T$ has a greater impact on the stiffness than on the mass of the actuator. However, at higher values of $L_p/L_T$, increasing $L_p/L_T$ has a greater impact on the mass than on the stiffness of the actuator. Thus, there is some length $L_p/L_T$ that balances these two competing effects. This gives an idea of the optimum piezoelectric patch length for maximizing the natural frequency of the present piezoelectric actuator.

Figure 11 shows the dc response comparison between experiment and theoretical models. All theoretical models predict the dc response to a reasonable accuracy of +/- 15%. The dc response increases monotonically with increasing piezoelectric length and saturates around a value of $L_p/L_T = 0.9$. It is clear that increasing the piezoelectric length induces more strain, which leads to larger tip displacements and hence a larger dc response. It can also be observed that the dc response predicted by the perfect bond finite element model nearly matches that predicted by the analytical model. Thus the experimental data presented here give confidence in the theoretical predictions by the models developed, with the shear lag finite element model being the most accurate, while the analytical model is the simplest.

The analytical and finite element formulation treats the actuators as a beam model. Actuator dimensions resemble that of a plate, which has less stiffness than a beam. Leissa [1993] defined a frequency parameter given by $\omega l^2 \sqrt{(12\rho/Et^2)}$, where $\omega$ is the natural frequency in radians, $l$ is the total length, $\rho$ is the density, $E$ is the elastic modulus and $t$ the thickness of a homogeneous cantilever plate. Approximating the actuator designs by homogeneous plates, and calculating the frequency parameters yielded values of 3.63. However the frequency parameter

value for a homogeneous cantilever beam is 3.52 (Thomson [1993]). Since the frequency

parameter values are within 3 %, approximating the actuator design by a beam model is justified.
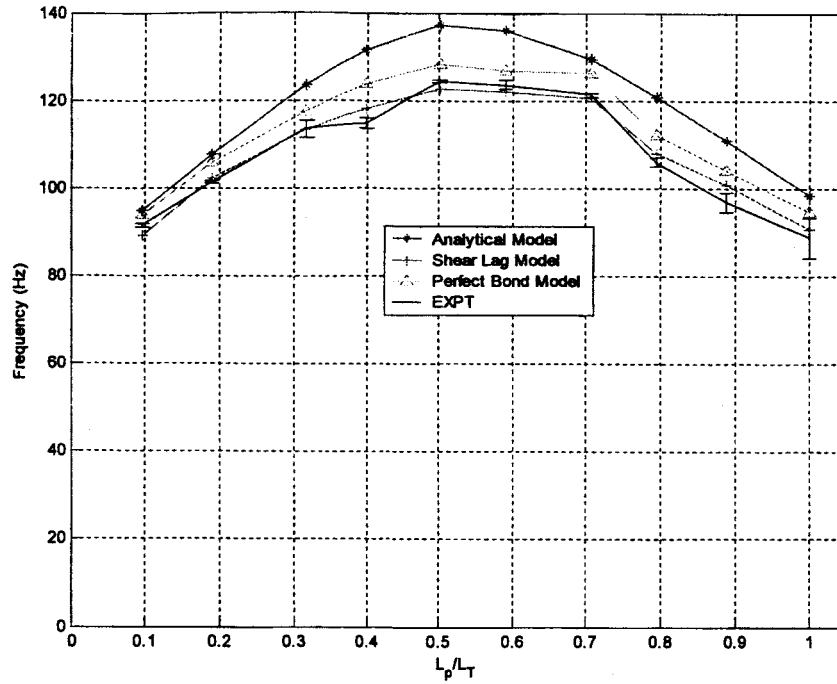


**Figure 10: Comparison of natural frequency between experiment and theory.**
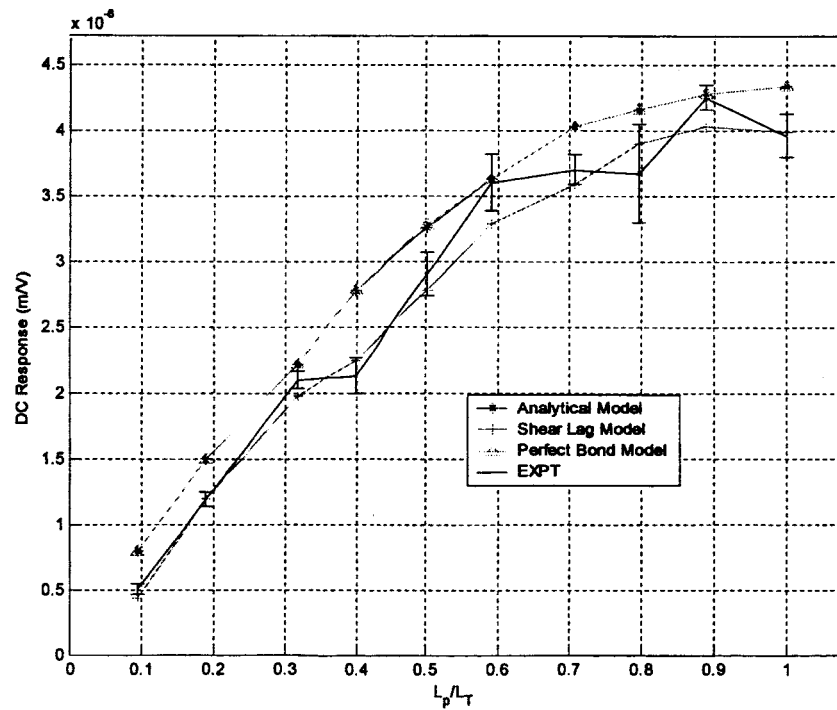


**Figure 11: Comparison of dc response between experiment and theory.**

## 3.7 Actuator Design Considerations

It can be observed from the experimental results that the dc response increases monotonically with the piezoelectric patch length and there is an optimum piezoelectric length that maximizes the system bandwidth. The study revealed the dependence of the dc response and the natural frequency of the actuator on only one parameter, the ratio of the piezoelectric patch length to the total length of the actuator, $L_p/L_T$. However, the analytical static analysis, described earlier, showed that the nondimensional dc response depends on non-dimensional parameters like $t_p/t_s$, $L_p/L_T$, $E_p/E_s$, $t_s/L_T$ and the nondimensional natural frequency is a function of non-dimensional parameters like $t_p/t_s$, $L_p/L_T$, $E_p/E_s$, and $\rho_p/\rho_s$.

A nominal design with $L_p/L_T = 0.5$, $t_p/t_s = 0.5$, $E_p/E_s = 0.85$, $t_s/L_T = 0.0073$, and $\rho_p/\rho_s = 2.48$ is selected to study the dependence of both non-dimensional dc response, $W$, and natural frequency, $F$, on the actuator parameters. Figure 12 (a-d) shows the variation of the non-dimensional dc response. For each plot only the parameter along the x axis is varied while all other parameters are fixed at their nominal value.

$W$ increases monotonically with the stiffness of the piezoelectric patch as well as its length, and saturates for a value of $L_p/L_T = 0.9$. However, $W$ increases initially as the thickness of the piezoelectric is increased until a value of $t_p/t_s = 0.54$, and then decreases on further increasing the thickness ratio. As $t_s/L_T$ ratio is increased, $W$ drops. The same behavior is shown by bimorph actuator in Figure 13 (a-d), only difference being that $W$ peaks at $t_p/t_s = 0.39$. Also as shown in plots 11 c) and 11 d), $W$ drops with increasing $t_s/L_T$ and increases with increasing $L_p/L_T$, until it saturates around a value of $L_p/L_T = 0.9$.

32

The variation of non-dimensional natural frequency with the design parameters for a unimorph is shown in Figure 14 (a-d). It can be seen that $F$ increases with increasing stiffness ratio and thickness ratio but drops with increasing density ratio. $F$ peaks at a length ratio of $L_p / L_T = 0.53$ and then drops on further increasing the piezoelectric patch length. The same behavior is exhibited by bimorph in Figure 15 (a-d). Here $F$ peaks for a length ratio of $L_p / L_T = 0.55$.
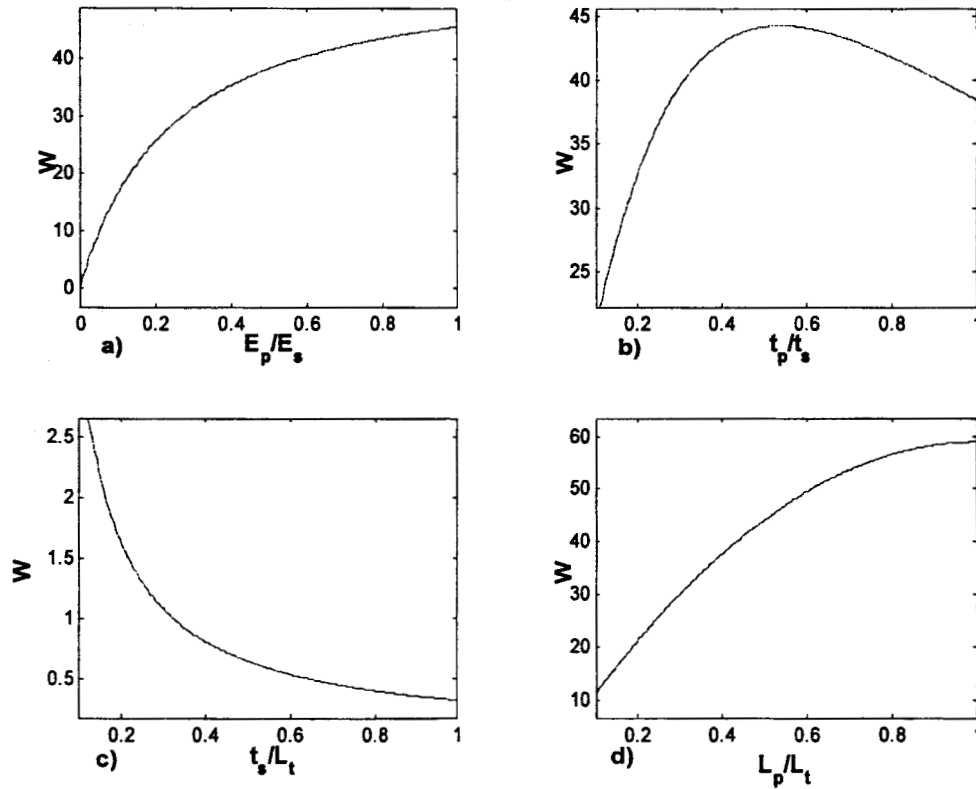


**Figure 12 (a-d): Variation of non-dimensional dc response with the design parameters for a unimorph.**
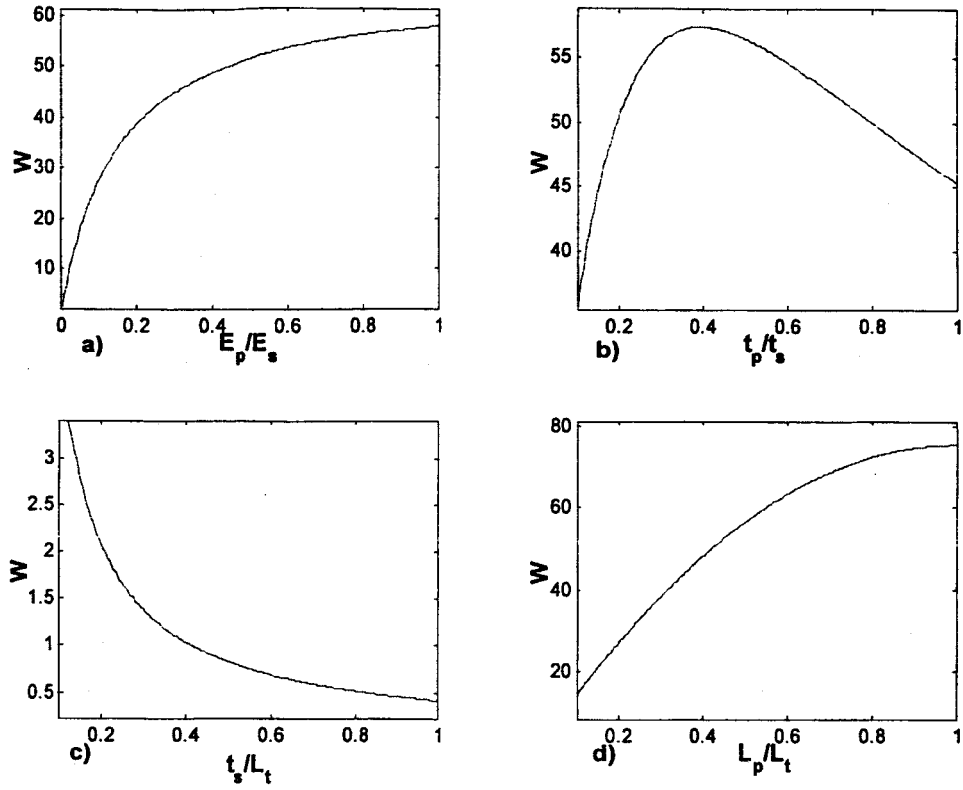
**Figure 13 (a-d):** Variation of non-dimensional dc response with the design parameters for a bimorph.
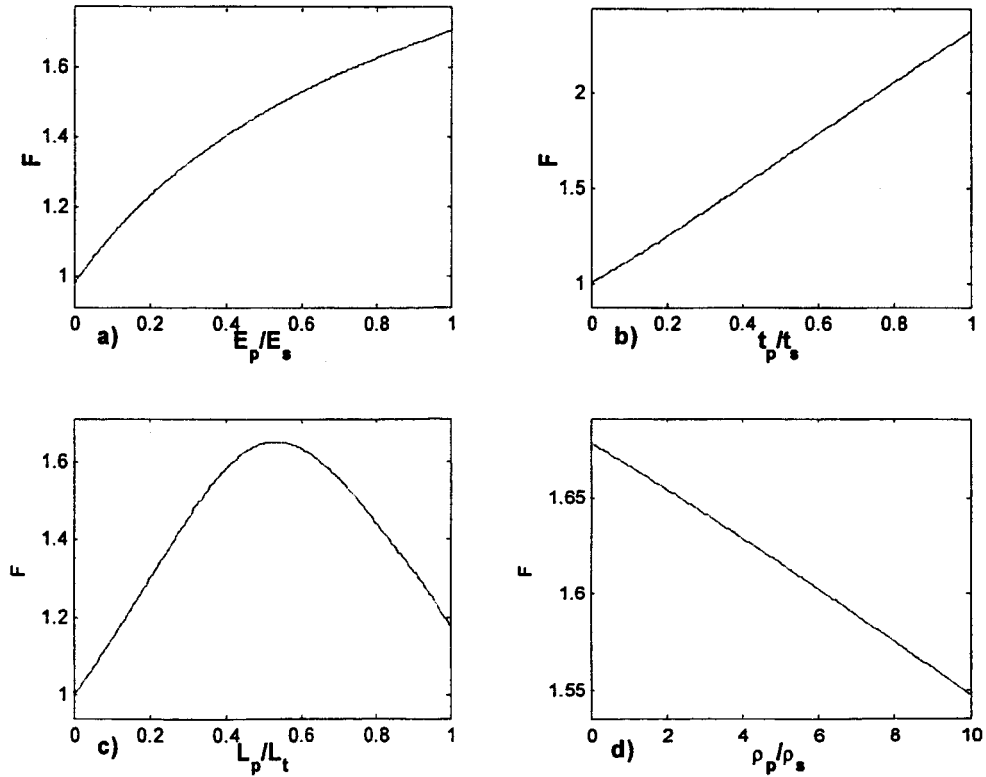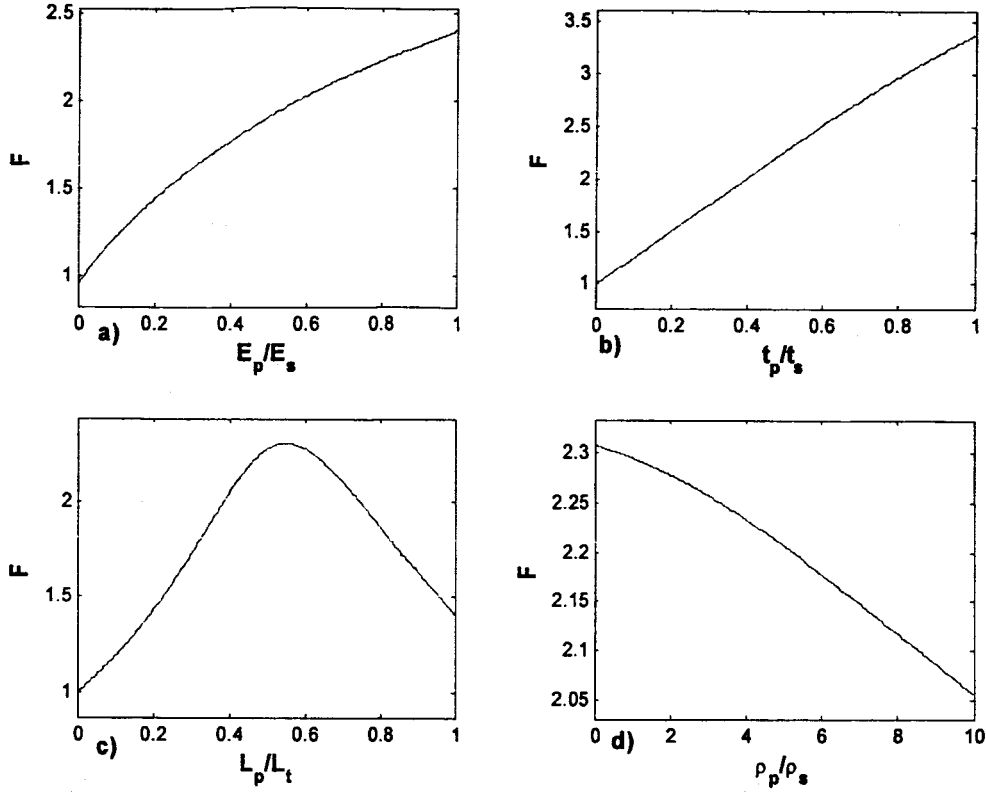


**Figure 14 (a-d):** Variation of non-dimensional natural frequency with the design parameters for a unimorph.

**Figure 15 (a-d):** **Variation of non-dimensional natural frequency with the design parameters for a bimorph.**

It is clear from the above plots that since the actuator performance depends on a number of design parameters, a design optimization has to be performed in order to develop an actuator that gives the best performance. We are specifically interested in designing an actuator that gives the maximum tip deflection for a given system bandwidth, which is approximated by the natural frequency of the actuator. Consider the case of one of the unimorph actuators developed that has a total length of 70 mm, piezoelectric patch length of 35 mm ($L_p / L_T = 0.5$), shim thickness of 508 µm, and piezoelectric thickness of 254 µm. The natural frequency of this actuator calculated from analytical scaling analysis is 137 Hz and its non-dimensional dc response, $W$ is 44.2. For the same total length ($L_T$), applied electric field ($V / t_p$), and the piezoelectric material constant ($d_{31}$) as this nominal actuator, we are interested in developing an unimorph actuator that will maximize the value of the non-dimensional dc response, $W$, while maintaining a minimum value

of the natural frequency at 137 Hz. This can be achieved by optimizing the piezoelectric thickness ($t_p$), the shim thickness ($t_s$), and the length of the piezoelectric patch ($L_p$). We are also interested in estimating the gain in $W$ that can be achieved by developing an optimized bimorph actuator that has the same total length, piezoelectric constant and the applied electric field as the nominal design, at the same frequency. Therefore an actuator optimization scheme based on Matlab® was implemented to maximize the non-dimensional dc response, $W$. The 'fmincon' function in Matlab® minimizes the cost function subject to a set of constraints on the actuator design parameters, thus giving the maximum attainable value for the cost function. The negative of non-dimensional tip deflection, $-W$ was chosen to be the cost function for the optimization. The cost function is expressed as,

$$-W = \frac{-w_{tip} t_p}{d_{31} V L_T} \cong \frac{3\bar{E}(1+\bar{t})\bar{t}(\bar{L}-2)\bar{L}\frac{L_T}{t_s}}{\left(1+4\bar{E}\bar{t}+6\bar{E}\bar{t}^2+4\bar{t}^3\bar{E}+\bar{E}^2\bar{t}^4\right)}.$$  (33)

Similarly, the cost function for the bimorph can be expressed as

$$-W = \frac{-w_{tip} t_p}{d_{31} V L_T} \cong \frac{6\bar{E}(1+\bar{t})\bar{t}(\bar{L}-2)\bar{L}\frac{L_T}{t_s}}{\left(1+6\bar{E}\bar{t}+12\bar{E}\bar{t}^2+8\bar{t}^3\bar{E}\right)}.$$  (34)

To gain more insight into the choice of optimization function, let us examine the terms on the LHS of Eq. (34) used to non-dimensionalize the tip deflection, $w_{tip}$. The piezoelectric constant $d_{31}$ is a constant for a given piezoelectric material. Similarly the total length of the piezoelectric actuators $L$ is also a constant. That leaves the electric field, $V/t_p$, where $V$ is the applied external voltage and $t_p$ is the thickness of the piezoelectric patch. It can be seen easily that maximum deflection can be achieved when the value of the electric field equals the value of the

36

coerecive field of the piezoelectric. Thus the choice of the optimization function $W$ or $w_{tip}$, is not crucial.

The design variables involved in the optimization are the thickness of the piezoelectric ($t_p$) and shim ($t_s$) as well as the length of the piezoelectric ($L_p$). An optimum design for an actuator that has a natural frequency value that is at least 137 Hz, is sought. This constraint can be represented in the mathematical form as

$$f_n > 137 Hz \tag{35}$$

The maximum patch length of the piezoelectric should not exceed the total length of the actuator and the design parameters should always be non-negative, giving rise to the remaining inequality constraints,

$$L_p \leq L_T \tag{36}$$

$$L_p > 0, \ t_p > 0, \ t_s > 0 \tag{37}$$

The optimization scheme seeks the values of $t_p$, $t_s$, and $L_p$ that maximizes the value of $W$. The result of the optimization study along with the result of the analytical static analysis of the nominal design is summarized in Table 2.

**Table 2: Results of the optimization study.**

| Parameter | Optimized Unimorph | Optimized Bimorph | Nominal design |
|-----------|-------------------|-------------------|----------------|
| $L_T$ | 70 mm | 70 mm | 70 mm |
| $t_s$ | 309 µm | 98.5 µm | 508 µm |
| $t_p$ | 404 µm | 305 µm | 254 µm |
| $L_p$ | 44.5 mm | 46 mm | 35 mm |
| $f_n$ | 137 Hz | 137 Hz | 137 Hz |
| $W$ | 63.1 | 127.9 | 44.2 |

It can be seen from the table that optimizing the design variables can increase $W$ 1.5 times the nominal design. The value of $W$ obtained from the optimized bimorph case is almost the double of that for the optimized unimorph. In order to validate the choice of the optimization function chosen, a separate optimization for a unimorph actuator was done where the cost function was $w_{tip}$ instead of $W$, with the additional constraint that $V/t_p = V_c$, where $V_c$ is the coercive field and has a value of 30 V/mil. The resulting tip deflection $w_{tip}$ had a value of 0.00142 m which is the same value for $w_{tip}$ obtained from optimizing $W$.

Thus, by constructing an actuator based on the optimized dimensions, maximum tip deflection can be attained for a prescribed natural frequency. This result is of particular importance in flow control applications, which makes use of large volume displacements of the actuator, while placing constraints of the bandwidth of generation.

## 3.8    Conclusions

An analytical static analysis, and two Finite Element Models, one using perfectly bonded shim and piezoelectric elements and the other using a shear element for the bond between the shim and the piezoelectric were developed and compared to tip displacement frequency response measurements of piezoelectric unimorph flaps. A parametric study was conducted in which the size of the piezoelectric patch was systematically varied from 10% to 100% of the entire beam length in approximately ten equal steps (while all other variables were fixed). The purpose of the study is to develop and validate a design tool, which will ultimately be used to design such actuators.

The dc response as well as the natural frequency of the actuators were extracted from the frequency response function plots and compared to that obtained from the models. All models predicted the dc response accurately. The analytical natural frequency served as an upper limit for the theoretical predictions, the best estimate of which was obtained by the shear lag model.

The benefit of the analytical model is that it describes the functional dependence of the non-dimensional dc response on design parameters like $t_p/t_s$, $L_p/L_T$, $E_p/E_s$, $t_s/L_T$ and the dependence of non-dimensional natural frequency on design parameters like $t_p/t_s$, $L_p/L_T$, $E_p/E_s$, and $\rho_p/\rho_s$ for both unimorph and bimorph actuators. The analytical model is much simpler than both the finite element models and it predicts the response to a reasonable accuracy of better than 15%. The analytical model was also used to formulate an optimization procedure that maximized the non-dimensional dc response, for a given system bandwidth.

An in-depth understanding of the structural dynamic characteristics of piezoelectric actuators will enable us to reliably utilize them in the design of actuators for flow-control applications. In

addition, the important question of coupling between the actuator and fluid motions can be rigorously studied.

## 3.9 Publications

Mathew, J., Sankar, B.and Cattafesta, L., "Finite Element Modeling of Piezoelectric Actuators for Active Flow Control Applications", AIAA Paper 2001-0300, 39th AIAA Aerospace Sciences Meeting and Exhibit, Reno, NV January 8-11, 2001.

Cattafesta, L., Mathew, J., and Kurdila, A., "Modeling and Design of Piezoelectric Actuators for Fluid Flow Control," SAE 2000 Transactions Journal of Aerospace, Section 1, Vol. 109, pp. 1088-1095, 2001.

Cattafesta, L. N., III, Garg, S., and Shukla, D. "The Development of Piezoelectric Actuators for Active Flow Control," AIAA Journal, Vol. 39, No. 8, pp. 1562-1568, August 2001.

Mathew, J., A theoretical and experimental study of piezoelectric unimorph actuators for active flow control, M.S Thesis, May 2002.

## 3.10 References

1. Crawley, E. F and de Luis, J. D., "*Use of Piezoelectric Actuators as Elements of Intelligent Structures*," AIAA Journal, Vol.25, No 10, pp. 1373-1385, 1987.

2. Cattafesta, L. N. III, Garg, S., and Washburn, A. E., "Piezoelectric Actuators for Fluid-Flow Control," Proceedings of the SPIE, 3044:147-157, March 1997.

3. Leissa, A., Vibration of Plates, Acuostical Society of America, Sewickley, 1993.

4. Thomson W. T., Theory of Vibration with Applications, 4th ed., Prentice Hall, Englewood Cliffs, 1993.

## Appendix A - FEM Formulation for the Shear Lag Model

A schematic of the model is shown in Figure A-1. The flap is discretized into $n_g$ elements in the gap region, $3n_c$ elements in the composite region (i.e., one each for the shim, bond, and piezo portions), and $n_s$ elements in the shim region.
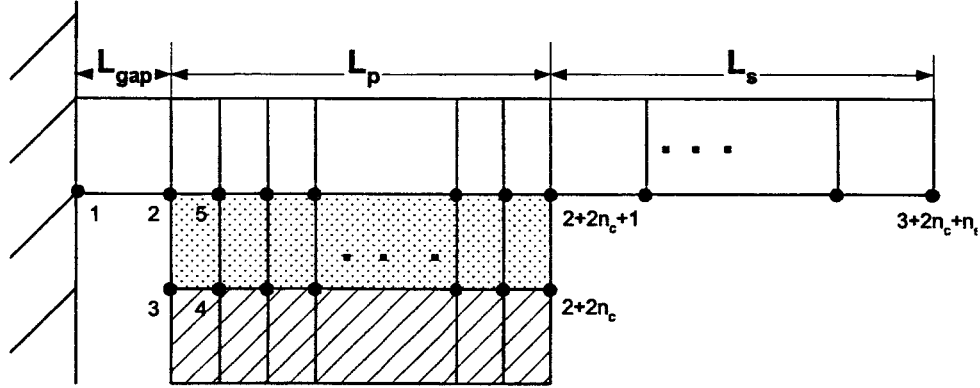


**Figure A-1: Node-numbering scheme for the finite-element, shear lag model.**

The piezo and shim elements are similar to the "Hermitian" beam elements used in the perfect bond FEM [Cattafesta et al. 2000], having 2 nodes and 3 degrees of freedom $(u, w, \theta)$ at each node. Here, $u$ is the horizontal or $x$ displacement of the nodes, $w$ is the vertical or $z$ displacement, and $\theta$ is the angular displacement. Each element in the bond layer has four nodes with two degrees of freedom $(u, w)$ at each node. In the perfect bond model, the nodes are defined at the midpoint of the element faces $(i', j', k', l')$. However as shown in Figure A-1, for the shear lag model, the nodes need to be offset downwards (upwards) for the shim (piezo) elements to allow these nodes to coincide with the four nodes of the bond element $(i, j, k, l)$. A schematic of the element nodes, degrees of freedom, and transformation is shown in Figure A-2.
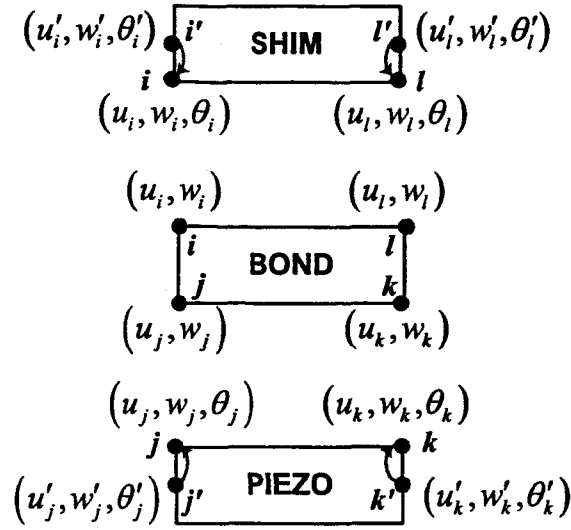
41

**Figure A-2: Schematic of the discretized flap elements.**

The node offset is achieved by defining a transformation matrix $T$

$$T = \begin{bmatrix} 1 & 0 & \pm\dfrac{t}{2} & 0 & 0 & 0 \\ 0 & 1 & 0 & 0 & 0 & 0 \\ 0 & 0 & 1 & 0 & 0 & 0 \\ 0 & 0 & 0 & 1 & 0 & \pm\dfrac{t}{2} \\ 0 & 0 & 0 & 0 & 1 & 0 \\ 0 & 0 & 0 & 0 & 0 & 1 \end{bmatrix} \tag{A.1}$$

where the "+" and "−" signs are used to shift the shim and piezo elements, respectively, and $t$ is the thickness of the element.

The elemental mass matrix is derived from the equation for kinetic energy of an element. For shim and piezo elements, the transformed elemental mass matrix is given by

$$m_e = T^T \bar{m} T \tag{A.2}$$

$$\overline{m} = \frac{ml}{420} \begin{bmatrix} 140 & 0 & 0 & 70 & 0 & 0 \\ 0 & 156 & 22l & 0 & 54 & -13l \\ 0 & 22l & 4l^2 & 0 & 13l & -3l^2 \\ 70 & 0 & 0 & 140 & 0 & 0 \\ 0 & 54 & 13l & 0 & 156 & -22l \\ 0 & -13l & -3l^2 & 0 & -22l & 4l^2 \end{bmatrix} \tag{A.3}$$

where the superscript "$T$" denotes "transpose," $m$ is the mass per unit length, and $l$ is the length of the element. The mass of an individual bond element is lumped into equal masses at the four nodes of the element, giving rise to an $8 \times 8$ diagonal matrix with $ml/4$ along the diagonal.

The element stiffness matrix is determined from the strain-energy relation. For the piezo and shim elements, it has the form

$$k_e = T^T \overline{k} T \tag{A.4}$$

$$\overline{k} = \frac{EI}{l^3} \begin{bmatrix} \dfrac{Al^2}{I} & 0 & 0 & \dfrac{-Al^2}{I} & 0 & 0 \\ 0 & 12 & 6l & 0 & -12 & 6l \\ 0 & 6l & 4l^2 & 0 & -6l & 2l^2 \\ \dfrac{-Al^2}{I} & 0 & 0 & \dfrac{Al^2}{I} & 0 & 0 \\ 0 & -12 & -6l & 0 & 12 & -6l \\ 0 & 6l & 2l^2 & 0 & -6l & 4l^2 \end{bmatrix} \tag{A.5}$$

where $E = \left( E_s \text{ or } E_p \right)$ is the elastic modulus, $A$ is the area, and $I$ is the moment of inertia about the local neutral axis. The elemental stiffness matrix for the bond layer is given by

$$k_e = \frac{bl}{2t_b} \begin{bmatrix} G & 0 & 0 & 0 & 0 & 0 & -G & 0 \\ 0 & E_b & 0 & 0 & 0 & 0 & 0 & -E_b \\ 0 & 0 & G & 0 & -G & 0 & 0 & 0 \\ 0 & 0 & 0 & E_b & 0 & -E_b & 0 & 0 \\ 0 & 0 & -G & 0 & G & 0 & 0 & 0 \\ 0 & 0 & 0 & -E_b & 0 & E_b & 0 & 0 \\ -G & 0 & 0 & 0 & 0 & 0 & G & 0 \\ 0 & -E_b & 0 & 0 & 0 & 0 & 0 & E_b \end{bmatrix} \qquad (A.6)$$

where $G$ and $E_b$ are the bond shear and elastic modulus, respectively, $l$ is the length, $b$ is the width, and $t_b$ is the thickness of the bond layer.

There are no external loads of interest acting on the shim and bond regions. However, for the piezo element, the load vector is given by

$$F_E = T^T F \qquad (A.7)$$

$$F = \begin{pmatrix} -d_{31} E_{field} E_p A \\ 0 \\ 0 \\ \vdots \\ d_{31} E_{field} E_p A \\ 0 \\ 0 \end{pmatrix} \qquad (A.8)$$

As usual, the elemental mass and stiffness matrices are then combined to obtain the global mass and stiffness matrices $M$ and $K$, and the boundary conditions are imposed. To include the effects of damping, we use Rayleigh proportional damping (see Thomson, p. 191 for details).

The frequency response of the actuator may then be calculated by assuming a solution of the form $Y = Y_0 e^{i\omega t}$ subject to harmonic forcing $F = F_0 e^{i\omega t}$, where $[Y_0]$ is the nodal displacement vector. The governing matrix equation becomes

$$M\ddot{Y} + C\dot{Y} + KY = F \qquad\qquad (A.9)$$

The solution to the undamped, free vibration problem is an eigenvalue problem

$$\left[K - \omega^2 M\right]Y_0 = 0 \qquad\qquad (A.10)$$

in which the natural frequencies of the beam are defined by the square root of the eigenvalues of

$$[K - \omega^2 M] \qquad\qquad (A.11)$$

The solution to the damped, forced vibration problem is given by the matrix solution

$$Y_0 = \left[K + i\omega C - \omega^2 M\right]^{-1} F_0 \qquad\qquad (A.12)$$

where $\omega$ is varied from zero to a specified frequency in discrete steps.